



1 Lidar studies on microphysical influences on the structure 2 and lifetime of tropical cirrus clouds

3 G S Motty^{1*}, Malladi Satyanarayana^{1,2}, G S Jayeshlal¹, and V P Mahadevan Pillai¹

4 ¹ Department of Optoelectronics, University of Kerala, Kariavattom, Trivandrum-695 581, Kerala, India

5 ² Geethanjali College of Engineering & Technology, Cheeryal (V), Keesara (M), R.R.Dist. Hyderabad-501 301,
6 India

7 *Correspondence to:* G S Motty (mottygs@gmail.com)

8
9 **Abstract.** An understanding of the role of ice crystals in the cirrus cloud is significant on the the radiative
10 budget of the planet and consequent changes in the temperature. The structure and composition of the cirrus is
11 affected by the microphysical parameters and size and fall speed of ice crystal inside the clouds. In this study,
12 the structure and dynamics of tropical cirrus clouds were analysed by the microphysical characterisation using
13 the data obtained by the ground based lidar system over the tropical site Gadanki [13.5° N, 79.2° E], India for a
14 period of 6 years from 2005 to 2010. The observed clouds have optical depth within the range 0.02 to 1.8, lidar
15 ratios are in the 20 to 32 sr range and depolarisation ratio varies between 0.05 and 0.45. The altitude and
16 temperature dependence of the parameters, their interdependence and the fall velocity – effective size analysis
17 were investigated. Dependence of the microphysical parameters on the ice fall velocity which is critical for
18 climate change was also analysed. The same are compared with the CALIPSO satellite based CALIOP lidar
19 observations.

20
21 **Keywords:** ground lidar; CALIPSO; cirrus optical depth; lidar ratio; depolarisation ratio; crystal shape; fall
22 velocity.

23 1. Introduction

24 In the high altitude cirrus clouds, ice crystals appear in a variety of forms and shapes, depending on the
25 formation mechanism and the various atmospheric conditions (Liou, 1986; Rogers, 1976; Heymsfield and Platt,
26 1984). In cirrus clouds, at temperatures lower than about -45° C, ice crystals form and exist as mainly
27 nonspherical particles (Petrenko and Whitworth, 1999). Moreover, high altitude clouds in the altitude range
28 between 8 to 20 km, have an important place in sustaining the energy budget (Wallace and Hobbs, 2006) of the
29 earth atmosphere system by interacting with solar radiation (Stephens, 1990). Ice clouds reflect solar radiation
30 effectively back to space, called albedo effect and absorb thermal emission from the ground and lower
31 atmosphere, through the greenhouse effect (Stephens, 1990). In spite of their occurrence high and temperature,
32 the microphysical conditions have fundamental implications in terms of radiative transfer (Liou and Takano,
33 2002). There for it is significant to analyse the microphysical properties of cirrus clouds including their structure
34 for estimating their radiative properties accurately (Cess et al., 1990).

35
36 Earlier extensive experimental studies analysed the importance of cirrus clouds in the radiation budget
37 using various techniques employing lidars (Liou, 1986; Prabhakara et al., 1988; Ramanathan et al., 1989; Sassen
38 et al., 1989; Wang et al., 1996; Hartmann et al., 2001; Stubenrauch et al., 2010; Motty et al., 2015, 2016).
39 Heymsfield and McFarquahar (1996) found that cirrus clouds distributed in the tropics and play an important
40 role in radiative effects. Prabhakara et al. (1993) suggested that the greenhouse effect produced by the optically



41 thin cirrus act as a significant factor in maintaining the warm pool. Heymsfield and Miloshevich (2003) have
42 shown that top of the cloud layers composed of thin ice crystals, whereas the lower parts consists more thick
43 crystals. Wang et al. (1994) and Stubenrauch et al. (2010) stated that tropical cirrus clouds have strong potential
44 to impact the tropical and global climate. Recent research by Kulkarni et al.(2008) and Vernier et al. (2015)
45 shows that aerosols in the tropical tropopause layer (TTL) act as ice condensation nuclei and is higher during
46 monsoon periods.

47 The vertical profiles on cirrus formations over a local station can be obtained from the ground based
48 lidar system while for global coverage observations using the Cloud Aerosol Lidar with Orthogonal Polarization
49 (CALIOP) onboard the Cloud Aerosol Lidar and Infrared Pathfinder Satellite Observation (CALIPSO) satellite
50 are widely used (Dessler et al., 2009; Meenu et al., 2010). During the last few years, significant efforts are being
51 pursued to study the cirrus characteristics using the ground based lidar system over the tropical station Gadanki
52 (Sivakumar et al., 2003, Parameswaran et al., 2003 and Krishnakumar et al., 2014), but mainly for deriving the
53 general features and their variations in different periods of the year. Sivakumar et al. (2003) found that the
54 various cirrus formations are closely related to the tropospheric temperature. Parameswaran et al. (2003) stated
55 that for the cirrus covered region, the decrease in the environmental lapse rate could possibly be attributed to the
56 cloud induced IR heating. Also according to Krishnakumar et al. (2014), a notable dependence is observed
57 between the ice crystal morphology in the clouds and the various dynamical conditions of the prevailing
58 atmosphere. Thus the ice composition and the microphysics of cirrus can be understood by using the lidar data
59 on their scattering properties in deriving the quantitative values of the extinction coefficient, optical depth,
60 depolarisation properties, lidar ratio, effective size of ice crystal and fall velocity in order to analyse the
61 radiative effects.

62 The major objective of this paper is to contribute towards improving the understanding of the radiative effects of
63 cirrus clouds in terms of their microphysical parameters over the Indian tropical station, Gadanki [13.5° N, 79.2°
64 E], using the ground based NARL lidar system and the Caliop observations on a seasonal mean basis along with
65 their interdependence. Cirrus cloud observations on 152 days during the period 2005-2010 were analysed using
66 the data from both the lidar techniques and the results obtained were compared with the earlier reports.

67 **2 Data sources and Analysis**

68 **2.1 Ground based lidar (GBL)**

69 The ground based data obtained from the lidar system installed at the National Atmospheric Research
70 Laboratory (NARL), Gadanki (13.5° N, 79.2°E) for the period (2005-2010). The further specification for the
71 ground based lidar system are the same as employed in Motty et al. (2015, 2016), and the following text is
72 derived from there with minor modification. The NARL lidar is a monostatic, biaxial dual polarisation system
73 which transmits Nd: YAG laser pulses of wavelength 532 nm at a rate of 20 Hz (50 Hz since 2007). Each pulse
74 has pulse energy of 550 mJ (600 mJ since 2007) and pulse duration of 7 ns. The laser beam emerging with a
75 divergence of 0.45 mrad from the source and to reduce the divergence to < 0.1 mrad before transmitting
76 vertically into the atmosphere, the beam is expanded using a 10X beam expander. The backscattered photons
77 from the atmosphere are collected by two independent telescopes. One of the telescopes is designed to collect



78 the backscattered photons from the air molecules above 30 km in the atmosphere (called Rayleigh receiver) and
79 the other is designed to collect the backscattered photons from altitude below 30 km to study aerosols and
80 clouds (called Mie-receiver). The Mie-receiver contains a Schmidt-Cassegrain telescope of 35.5 cm diameter
81 with a field of view of 1 mrad. In order to eliminate the unwanted background noise from the received signal, a
82 narrow band interference filter with wavelength centred at 532 nm and a full-width at half-maximum of 1.1 nm
83 is placed in front of a polarizing beam-splitter. The polarizing-beam splitter splits the beam into parallel and
84 perpendicularly polarized beams which are then detected by two identical orthogonally aligned photomultiplier
85 tubes. The counting system consists of a Multi-Channel Scalar card and the photon counts are accumulated in
86 300m resolution bins and integrated for 4 min. Lidar data were collected only during the nights that are free
87 from low-level clouds and rain.

88 2.2 Satellite based lidar (SBL)

89 The CALIOP onboard the CALIPSO satellite provides high- resolution observations of the vertical distribution
90 of clouds and aerosols and their optical properties along the satellite track (Winker et al., 2007). The following
91 description about the lidar system is obtained from Motty et al., (2015, 2016) with minimal changes. In order to
92 compare the properties of cirrus clouds obtained from NARL lidar, level-2, 5 km cloud layer and cloud profile
93 data of product version 3 obtained for a grid (5° N - 20° N; 60° E - 85° E) during the period of June 2006–
94 December 2010 was used (Motty et al.,2016). CALIOP is a near-nadir viewing space-based, dual-wavelength,
95 dual-polarization, three channel elastic backscatter lidar that transmits linearly polarized laser pulses having an
96 average pulse energy of 110 mJ both at first (1064 nm) and second harmonic (532 nm) wavelengths of Nd:
97 YAG laser (Winker, 2003; Hunt et al., 2009; Winker et al., 2009; Pandit et al., 2015; Motty et al.,2016). The
98 backscattered signal is received by a 1m diameter telescope with parallel and perpendicularly polarized channels
99 at 532 nm wavelengths and one parallel channel at 1064 nm (Winker et al., 2007). The present study utilizes
100 version 3 of the level-2 cloud layer data product from CALIOP, where the data is gridded at 5 km horizontal
101 resolution. The data used in this work have a vertical and horizontal resolution of 60 m and 1000 m respectively
102 in the altitude region between 8.2 and 20.2 km.

103 In order to obtain the properties more accurately, simultaneous observations using ground-based and
104 space-borne lidar over a tropical station with opposite viewing geometry, night-time data collected when the
105 CALIOP overpasses nearby the Gadanki region were only considered. Because of the Caliop's repeat cycle of
106 16 days, four overpasses at most can be obtained in each month, with 2 each daytime and night-time overpass.
107 During the observation period a total number of 152 data files were collected from the NARL lidar system (
108 Motty et al.,2016) and 116 data files (Caliop observations are available from 2006 June onwards) from the
109 nocturnal observations obtained using CALIOP in the region selected around Gadanki. In this study the Calipso
110 observations with cloud top altitude greater than 8 km and those with CAD score in the range of 80–100 were
111 only considered.

112

113 2.3 Method of analysis

114 Fernald's inversion method is used to derive the extinction coefficient for the ground based NARL lidar data in
115 the region up to 20 km. The methods are the same as employed in Motty et al.,(2016) . Cloud optical depth



116 (COD, τ_c) is calculated by integrating the extinction coefficient from cloud base to its top and is an important
117 parameter depends on the composition and thickness of the cloud. The following estimations of τ are obtained
118 by Sassen et al. (1992) from their visual appearance: $\tau_c \leq 0.03$ for sub visible, $0.03 < \tau_c \leq 0.3$ for thin, $\tau_c > 0.3$
119 for dense cirrus clouds. The depolarisation ratio, $\delta(r)$ within the cloud indicates the phase of the cloud and
120 thereby to identify the type of ice crystals present within the cloud. Most of the tropical cirrus clouds are
121 composed of non-spherical ice crystals and will cause significant depolarisation. The lidar ratio (s_c) depends on
122 the structure and properties of ice crystals within the cirrus and as such it is range dependent. The range
123 dependent lidar ratio is obtained using the method suggested by Satyanaryana et al. (2010).

124 Also the Caliop parameters of cloud layers are obtained directly from CALIOP 5 km cloud layer data products.
125 The extinction coefficient as well as the IWC depends upon the particle size distribution of the clouds. The IWC
126 can be determined from the extinction measurements by using the relation provided by Heymsfield et al. (2005).
127 The effective diameter provides additional information for the ice cloud radiative characteristics and can be
128 obtained from the equation by Heymsfield et al. (2014) as a function of IWC, σ and the density of solid ice (ρ).

129 In order to analyse the fall velocity of ice crystals in terms of effective size, an aerodynamic equation
130 suggested by Mitchell et al., (1996) was employed.

131 **4 Results and discussion**

132 **4.1. Microphysical statistics of tropical cirrus**

133 The extinction coefficient, optical depth, lidar ratio and depolarization ratios are considered to be of special
134 importance since they are related to microphysics of the ice crystals contained on cirrus clouds. The
135 microphysical properties as well as the mid cloud altitude and temperature of the cirrus clouds together play an
136 important role in the radiative properties (Sunil kumar et al., 2008; Seifert et al., 2007). Here the climatology of
137 the cirrus over the tropical station Gadanki covering 152 days of lidar observations from 2005 to 2010 were
138 analysed. The observation period is divided into the prominent seasons of the Indian subcontinent namely winter
139 (December, January, February), summer (March, April, May), South West monsoon (June, July, August) North East
140 monsoon (September, October, December).

141 **4.1.1. Extinction coefficient**

142 The extinction coefficient (σ) provides the information on the influence of scatters on the radiation. Figure 1
143 shows the contour plot of seasonal variation of σ derived from ground based as well as satellite based lidar
144 observations.

145 It can be seen that there is significant variation in the values of σ during the period of observations for ground
146 based system. It is found that the σ value ranges between 5.0×10^{-3} to $8.91 \times 10^{-6} \text{ m}^{-1}$ and it is noted to be
147 highest during summer season having the range of value 1.5×10^{-4} to $1.7 \times 10^{-6} \text{ m}^{-1}$. During winter the σ value is
148 in the range of 2.0×10^{-6} to $2.5 \times 10^{-5} \text{ m}^{-1}$ range. The σ value during South-West Monsoon period is found to
149 be higher than North East Monsoon period having σ value ranges between 1.5×10^{-6} to $1.7 \times 10^{-4} \text{ m}^{-1}$ and 1.0
150 $\times 10^{-6}$ to $1.5 \times 10^{-5} \text{ m}^{-1}$ respectively. The satellite based Caliop lidar results also show similar behaviour and



151 the σ values ranges between 1.7×10^{-4} to $7.8 \times 10^{-6} \text{ m}^{-1}$. During the summer period σ ranges from 5.8×10^{-4} to
152 $4.6 \times 10^{-3} \text{ m}^{-1}$ and during winter from 4.5×10^{-4} to $3.6 \times 10^{-3} \text{ m}^{-1}$. Similar to ground based observation during
153 south west monsoon, Caliop observation also shows higher σ during south west monsoon period than the north
154 east monsoon periods having values ranges from 6.2×10^{-4} to $5 \times 10^{-3} \text{ m}^{-1}$ and 3.9×10^{-4} to $3.1 \times 10^{-3} \text{ m}^{-1}$
155 respectively.

156 Figure 2(a & b) shows the trend of the variation of average extinction coefficient with mid cloud height and
157 temperature from both observation techniques. In both cases the observed σ value does not show any clear
158 altitude dependence, but from the figure (2a), it is clear that most of the clouds formations in the altitude range
159 13-15 km range from both observation techniques. The figure (2b) shows the temperature dependence of σ
160 values and the points represent the average value of σ with mid cloud temperature and it can be seen that
161 σ decreases with the temperature and the most favourable cirrus occurring temperature ranges between -70 to -
162 55°C .

163 4.1.2. Optical Depth

164 The statistics of seasonal variation of optical depth by the two measurement techniques are shown in
165 figure 3.

166 The contour plot of seasonal variation of cirrus optical depths distribution for each season is depicted in
167 the figure 3. From fig. 3(a), 59% of the observed clouds were optically thin clouds with $\tau < 0.3$, 33% were sub-
168 visual clouds with $\tau_c < 0.03$ and only 8% were thick clouds with $\tau > 0.3$. Also in the region of 14 km and above,
169 where the cloud frequency is high, it is noted that 50% of clouds were sub-visual ($\tau_c < 0.03$) and 36% were
170 optically thin ($\tau_c < 0.3$) and the remaining are thick clouds. During the summer season τ ranges within 0.005 to
171 1.4 and during winter from 0.005 to 1. During the south west monsoon period, most of the observed τ values
172 are for thin clouds ranges between 0.01 and 1, and thick clouds were observed in all other seasons. North east
173 monsoon clouds give the τ within 0.002 to 0.87. The uncertainty related to cloud optical depth estimation from
174 CALIPSO data is less than 50% (Winker et al., 2007). The CALIPSO observations show that these clouds have
175 an average optical depth 0.15-1.7km. Figure 3(b) shows that from the satellite observation, 44% of the observed
176 clouds were optically thin clouds and the rest were thick clouds. The 80% of the observed clouds during the NE
177 monsoon period were optically thin. The seasonal optical depth distribution behaviour shows the same pattern in
178 the range 0-1km distributed over the observation periods for the two measurement techniques. The monsoon
179 periods have clouds with high optical depth in ground based measurement but the values are less when
180 compared to CALIPSO measurement. This may be due to the higher convective activities at tropics during the
181 monsoon periods.

182

183 The scatter plot of variation of optical depth with mid cloud height and temperature are shown in Fig.
184 4(a & b). From the height dependence of optical depth (fig. 4(a)), it can be inferred that optical depth increased
185 with the cloud height in the 11-15-km range and then decreases. Generally, the cirrus clouds that exist in the
186 tropopause region are optically thin (Nee et al., 1998). Figure 4(b) shows the temperature dependence of optical
187 depth and from that most of the thin clouds are having low temperature (below -68°C) and cloud formations are
188 widely observed in the range -70°C to -55°C . As the temperature increases the optical depth also increases. The
189 clouds observed in the tropical tropopause region are having an average temperature of $\approx 75^\circ \text{C}$, are normally



190 optically thin (Nee et al., 1998). Also it demonstrates a slightly positive dependence with the mid cloud
191 temperature which disagree with Wang et al. (2013) but in agreement with results of Sassen et al. (1992) which
192 shows a positive dependence with the mid cloud temperature.

193 4.1.3. Lidar Ratio

194 The correct values of extinction to back scatter ratio, commonly known as lidar ratio depicts the idea of
195 ice crystals in the cirrus clouds and reflect the cloud characteristics in the corresponding height region (Das et
196 al., 2009; Chen et al., 2002). According to Heymsfield and Platt (1984), in cirrus clouds at temperatures $\leq -50^{\circ}\text{C}$
197 and altitude 12 km contains different kinds of ice crystals.

198 Figure 5 shows the contour plot of seasonal distribution of lidar ratio during the period of observation.
199 Above 12 km, the lidar ratio values are mainly distributed between 20 to 30 sr ranges. During monsoon periods,
200 LR shows relatively higher values which varies between 20-27sr. By the satellite based observation, the LR
201 values varies between 24-32 sr and during NE monsoon periods, all the observed values are in the range 25-26
202 sr. The calculated lidar ratio can be compared with the previously reported results. Grund and Eloranta (1990)
203 reported the LR values about 15–50 sr using high spectral resolution lidar during the FIRE field. Sassen and
204 Comstock (2001) calculated the mean mid-latitude LR as $\sim 24 \pm 38$ sr with a median value of ~ 27 sr using
205 LIRAD. Pace et al. (2002) found the mean LR as $\sim 19 \pm 33$ sr for the equatorial cirrus. Also Seifert et al. (2007)
206 derived the mean LR during monsoon over tropics and derived a mean value of 32 ± 10 sr. Giannakaki et
207 al. (2007) derived LR as 28 ± 17 sr for mid-latitude cirrus. Das et al. (2009) determined the mean LR value of
208 23 ± 16 sr by using the simulation of lidar backscatter signals. Statistically; the above results are in agreement
209 with the present study.

210 Figure 6 (a) shows that the lidar ratio varies with mid cloud height randomly. It was found that within 12.5-15
211 km, the lidar ratio values are distributed mainly between 20- 28. The lower and higher clouds shows relatively
212 smaller LR values and over 13.5-14.5 range, higher LR values of the range 28-32 sr were observed. This
213 indicates that most of the observed clouds consist of hexagonal type crystals (Sassen et al., 1992) for both
214 observations. As in Fig. 6(b), lidar ratio appears to vary with mid cloud temperature with no clear tendency.
215 This can be due to the variations in the ice crystal properties at the particular temperature range or may be due to
216 the heterogeneous cloud formations over the region (Das et al., 2009). But in some cases, high LR values are
217 observed at lower temperature region which indicates the presence of thin cirrus clouds.

218 4.1.4. Depolarisation Ratio

219 Depolarisation ratios are influenced by the inhomogeneity of ice particles in cirrus clouds in the lidar
220 analysis. The depolarisation values for the water droplets are smaller rather than the ice particles. Figure 7
221 shows the seasonal distribution of depolarisation ratio and their height dependence and the wide range of
222 variation observed can be due to the heterogeneous nucleation process of cirrus, which results in different cloud
223 composition or may be due to the aspect ratio changes (Das et al., 2009). For ground based measurements, the
224 depolarisation ratio ranges within 0.04-0.45 as in fig.7(a) and 0.3-0.5 for satellite based measurement techniques
225 as in fig.7(b) and in both cases, maximum values are shown during summer period. Between 11-16km range,
226



227 the higher depolarisation values are observed (Motty et al., 2016) and above 16 km, smaller values < 0.2 are
228 observed may be due to the presence of super cooled or mixed phase of water (Sassen, 1995) and the
229 horizontally oriented ice crystals increases the same (Platt et al., 1978). The NARL Lidar observation showed
230 that during winter periods depolarisation varies between 0.05-0.3 and for monsoon periods it is 0.04-0.3. The
231 highest depolarisation values are observed during the summer periods. The depolarisation variation by the
232 satellite observation varies in the range 0.3-0.5 and for summer all observed values were higher and show
233 relatively lower values during NE monsoon periods. During monsoon, since the cloud condensation nuclei are
234 relatively higher the water content is more in the clouds.

235 Figure 8(a) presents the scatter plot of the dependence of average value of depolarization ratio on the mid cloud
236 height and the values are found to be scattered for both the measurement techniques; but an increasing tendency
237 is observed between 10-16 km. In most of the cases, depolarization ratio values ranges within 0.05 to 0.45.
238 Figure 8(b) shows depolarisation ratio plotted as a function of mid cloud temperature and most of the ice clouds
239 having depolarisation values above 0.3 show an increasing tendency with decreasing temperature within -80 to
240 -30 °C (Motty et al., 2016). For water clouds, depolarisation values ranges between 0-0.09 and it doesn't show
241 any temperature dependence. Since at higher altitude region, the cooler cirrus clouds are having bigger sized ice
242 crystals results higher depolarisation values and are in agreement with by Chen et al. (2002).

243 4.2. Interdependence of the optical properties

244 The dependence of microphysical characteristics of cirrus clouds over Gadanki were further investigated.
245 Figure 9(a) depicts the scatter plot of optical depth variation with lidar ratio. The lidar ratio of thin cirrus was
246 observed in 14-28 sr range and has the maximum value obtained at an optical depth range between 0.05 and 0.3,
247 which agrees with Wang et al. (2013). As the optical depth increases (thick clouds), the lidar ratio decreases and
248 is more clear in the satellite based observation. Also most of the optically thin cirrus shows lower lidar ratio
249 values. The variation of depolarisation ratio with optical depth is shown in figure 9(b) and from that clouds
250 having large depolarisation values are observed with smaller optical depth. From the figure, it is clear that the
251 sub-visual clouds show higher depolarisation values. The points with lower optical depth and higher
252 depolarisation values indicate the presence of thin cirrus clouds. In both the observation techniques, the points
253 denoting higher optical depth and higher depolarisation ratios show the occurrence of thick cirrus clouds. The
254 points with smaller depolarisation values are for water clouds. Some of the previous studies revealed a relation
255 between the particle depolarization ratio and particle lidar ratio, but found differing interdependencies.
256 According to Reichard et al. (2002), the particle depolarization ratio splits into two branches and with increasing
257 particle lidar ratio values, the difference of these two branches decreases. According to Chen et al. (2002), the
258 particle depolarization ratio splits into two branches, but with increasing particle lidar ratio values, the
259 difference of these two branches increases. Later by Sakai et al. (2006), the values for particle depolarization
260 and particle lidar ratio are enclosed between two vertices and are possible to distinguish the phase and
261 orientation of randomly oriented ice crystals by measuring the particle depolarization and particle lidar ratio.
262 Figure 9(c) shows the relation between depolarisation ratio and lidar ratio. For the present study, it does not show
263 any particular dependence.

264 According to the hexagonal crystal classification by Sassen et al. (1992), the observed data can be classified as
265 in fig.10. Here for the ground based observation, 51.20% of the cloud containing hexagonal thin plate ice



266 crystals, 30% were hexagonal thick plate crystals and 18.8% were long column type. From the satellite
267 observation, 52.8% of the cloud crystals were long column, 42.1% were thin plates and only 5.2% were thick
268 plate type crystals. The probable size and shape distribution of ice crystals in the cirrus clouds can be further
269 analysed clearly by calculating the effective diameter and fall velocity analysis.

270 4.3 Effective diameter and fall velocity analysis

271 Das et al. (2010) obtained the possible ice crystal formations with respect to the fall velocity – effective
272 diameter relation derived by Mitchell (1996). Here the average value of effective diameter is obtained using the
273 equation by Heymsfield et al. (2014) as a function of IWC, σ and the density of solid ice (ρ) and according to
274 the diameter obtained, the possible shapes are selected as suggested by Mitchell (1996). The obtained effective
275 diameters were estimated by averaging the diameter obtained during each season for the observed year. In the
276 present observation, ice crystals of various shapes, mainly hexagonal plates (HP) ($15 \leq D \leq 100$ and $100 \leq D$
277 ≤ 3000) and hexagonal columns (HC) ($100 \leq D \leq 300$ and $D > 300$) have been analyzed and the fall velocity is
278 obtained using their corresponding equations obtained by Das et al. (2010). These obtained ice crystal shapes are
279 similar to the previous classification as by Sassen et al. (1992) and are commonly found in cirrus clouds. The
280 seasonal average of the obtained parameters by the two measurement techniques are summarized as in Table
281 1 and 2.

282 Several earlier studies reported the size of most of the cirrus ice crystal to be about several hundred microns and
283 falls with velocity between 30 and 100 cm/sec (Mitchell, 1996; Heymsfield, 2003; Deng and Mace, 2008; and
284 Das, 2010). The results of the present study are in agreement with the previously obtained values.

285 The effective size of ice crystals in cirrus usually increases with mid cloud temperature as in figure 11 indicates
286 the presence of smaller sized ice crystals at lower temperature region. The lower temperature has been suggested
287 for homogeneous ice nucleation (Kärcher and Lohmann, 2002). The results obtained are similar for both the
288 ground based and satellites based observation techniques and are in agreement with Das et al. (2010),
289 Heymsfield et al. (2000), and Chen et al. (1997).

290

291 The fall velocity, the rate at which an ice crystal falls through a cloud, is dependent on its mass, size and shape
292 and thus can be used for effective size analysis. From the scatter plot of fall velocity variation with the mid
293 cloud temperature as in figure 12, the fall velocity is found to be broadly distributed and show an increasing
294 tendency with temperature. This is in agreement with the results obtained by Das et al. (2010) observed over
295 Chung-Li using the lidar measurements. As depicted in figure 12(b), the fall velocity varies linearly with the
296 effective size of cirrus crystal. Figure 12(c) shows the dependence of fall velocity on the cirrus optical depth
297 measurements. For larger ice crystals, the chances for homogeneous nucleation are lesser and the sedimentation
298 rate increases. The smaller sized crystals having low fall velocities undergo homogeneous nucleation processes
299 and thus the cloud remains for longer in the upper atmosphere. Also the water vapour in that region is higher
300 and it acts as a blanket and prevents long-wave radiation being emitted by the Earth from escaping into space,
301 enhancing warming. The effective size distribution of ice particles which decides the lifetime of the cirrus
302 clouds has strong impacts on the cloud radiative forcing due to its influence on cirrus cloud coverage. Here, the
303 fall velocity of cirrus ice crystals observed are relatively high, which may indicate that the ice particles will fall



304 out rapidly. Therefore, it can be said that the lifetime of the cirrus clouds in the tropics will dissipate faster and
305 causes LW dominance and thus have a significant effect on the radiation budget.

306 **Conclusion**

307 The important microphysical properties such as extinction coefficient, optical depth, lidar ratio and
308 depolarisation ratio for cirrus clouds obtained during 2005-2010 were analysed using the observations made by
309 the ground based lidar system at NARL Gadanki (13.5° N, 79.2° E) and are compared with the available night
310 time observations from the CALIOP on board the CALIPSO satellite. The dependence between these quantities
311 and its relationship with mid cloud height and mid cloud temperature were also obtained. The radiative effects
312 of obtained cirrus clouds were discussed by the effective size – fall velocity analysis of the cirrus ice particles.
313 The inter comparison of measurements by the two techniques showed that the satellite measurements match
314 very closely with the ground based data. However, small differences were noticed since the observations were
315 not being exactly obtained at the same place and the sampling frequencies were also different. Some of the
316 generally observed results from both observation techniques are listed which are as follows:

317

- 318 • The cirrus extinction coefficient ranges from 5.0×10^{-3} to $8.91 \times 10^{-6} \text{ m}^{-1}$ and 1.7×10^{-4} to 7.8×10^{-6}
319 m^{-1} for ground based and satellite based measurements respectively and it decreases with the
320 temperature.
- 321 • Cirrus optical depth varies from 0.02 to 1.8 ranges with most frequent occurrence being in the range
322 0.04 to 0.3. It was noted that optical depth increases with temperature of the mid cloud within the range
323 -50°C to -70°C and decrease with temperature outside this range. Within 11-15km range, the optical
324 depth increases with height and decreases for higher altitudes.
- 325 • The lidar ratio varies with mid cloud height randomly, and within 10 to 20 km the lidar ratio values are
326 distributed in the range 20 to 32 sr. The lower and higher clouds show relatively smaller LR values and
327 within 13.5 to 14.5 range higher LR values of the range 28 to 32 sr were observed. Lidar ratio varies
328 with the mid cloud temperature with no clear trend.
- 329 • Depolarization ratio was observed to increase from 0.05 to 0.45 with height between 10 and 16 km and
330 tend to decrease with the temperature varying from -80 to -30°C .
- 331 • Most of the optically thin cirrus shows lower lidar ratio values and are scattered among 14-28 sr range.
332 As the optical depth increase (thick clouds), the lidar ratio decreases.
- 333 • The clouds having large depolarisation values are with lower optical depth. Thin cirrus have lower
334 optical depth ($\tau \leq 0.3$) and higher depolarisation values (0.3 to 0.35) whereas the higher optical depth
335 ($\tau > 0.3$) and higher depolarisation ratios (0.35 to 0.45) shows the occurrence of thick cirrus clouds and
336 also the smaller depolarisation values (below 0.1) are for water clouds.
- 337 • The presented results are used to understand possible hexagonal crystal formations inside clouds using
338 the depolarisation ratio- lidar ratio analysis. The ground based measurements gives the occurrence of
339 more hexagonal thin plate crystals (51.20 %) during the observation whereas the satellite based
340 measurements shows the presence of higher long column crystal formation (52.80 %).



- 341 • The effective size of the ice crystal is lower at colder temperature and thus showing the large size at the
342 warmer temperature.
- 343 • The fall-velocity of the ice crystals increases with temperature, indicating the influence of particle
344 growth in cirrus coverage. The higher values of ice crystal fall velocity in cirrus clouds observed
345 indicate rapid fall out of the ice particles which causes the faster dissipation of cirrus clouds over
346 tropics causes the LW dominance and thus have a significant effect on the radiation budget.
- 347 • The detailed study on the influence of the possible hexagonal crystal formation on the characterisation
348 of radiative properties can be pursued in future.
- 349 • The results obtained on various microphysical properties of cirrus and their interrelationship along with
350 a comparative study of GBL and SBL data are expected to be useful in the radiative budget analysis.

351 **Acknowledgments**

352 The authors thank the National Atmospheric Research Laboratory, Department of Space, Government of
353 India, Gadanki, Tirupati, India for providing lidar data and also acknowledge the assistance given by NASA
354 Langley Atmospheric Science Data Centre for providing CALIPSO data.
355

356 **References**

- 357
- 358 1. Liou, K.-N.: Influence of Cirrus Clouds on Weather and Climate Processes: A Global Perspective,
359 *Mon. Weather Rev.*, 114, doi: 10.1175/1520-0493(1986)114<2.0.CO;2, 1986.
- 360 2. Rogers, R. R.: *A Short Course in Cloud Physics*. Pergamon Press, 227 pp., 1976.
- 361 3. Heymsfield, A. J. and Platt C. M. R.: A parameterization of the particle size spectrum of ice clouds in
362 terms of the ambient temperature and the ice water content, *J. Atmos. Sci.*, 41, 846–855, 1984.
- 363 4. Petrenko, V.F., and Whitworth, R.W.: *Physics of Ice*. Oxford University Press, 373 pp., 1999.
- 364 5. Wallace, J. M. and Hobbs, P. V.: *Atmospheric Science: An Introductory Survey*, Academia Press, MA,
365 USA, 2006.
- 366 6. Stephans, G.L., Tsay, S.C., Stackhous W.S., and Flatau, P.J.: The relevance of the microphysical and
367 radiative properties of cirrus clouds to climate and climatic feedback, *J. Atmos. Sci.* 47(14), 1742-
368 1754, 1990.
- 369 7. Liou, K.N. and Takano, Y.: Interpretation of cirrus cloud polarization measurements from radiative
370 transfer theory, *Geophys. Res. Lett.* 29, 2002.
- 371 8. Cess, R.D. and Coauthors: Intercomparison and interpretation of climate feedback processes in 19
372 atmospheric general circulation models, *J. Geophys. Res.*, 95, 16 601–16 615, 1990.
- 373 9. Prabhakara, C., Fraser, R. S., Dalu, G., Wu, M.-L. C., and Curran, R. J.: Thin cirrus clouds: Seasonal
374 distribution over oceans deduced from Nimbus-4 IRIS. *J. Appl. Meteor.*, 27, 379–399, 1988.
- 375 10. Ramanathan, V., Cess, R. D., Harrison, E. F., Minnis, P., Barkstrom, B. R., Ahmad, E., and
376 Hartmann, D.: Cloud-radiative forcing and climate: Results from the Earth radiation budget experiment,
377 *Science*, 243, 1-140, 1989.



- 378 11. Sassen, K., and Dodd, G. C.: Haze particle nucleation simulation in cirrus clouds, and applications for
379 numerical and lidar studies, *J. Atmos. Sci.*, 46, 3005–3014, 1989.
- 380 12. Wang, P.-H., Minnis, P., McCormick, M. P., Kent, G. S. and Skeens, K. M.: A 6 year climatology of
381 cloud occurrence frequency from stratospheric aerosol and Gas Experiment II observations (1985-
382 1990), *J. Geophys. Res.*, 101, 29407–29429, 1996.
- 383 13. Hartmann, D. L., Holton, J. R. and Fu, Q.: The heat balance of the tropical tropopause, cirrus, and
384 stratospheric dehydration, *Geophys. Res. Lett.*, 28(10), 1969–1972, 2001.
- 385 14. Stubenrauch, C. J., Cros, S., Guignard, A., and Lamquin, N.: A 6-year global cloud climatology from
386 the Atmospheric InfraRed Sounder AIRS and a statistical analysis in synergy with CALIPSO and
387 CloudSat, *Atmos. Chem. Phys.*, 10, 7197–7214, doi:10.5194/acp-10-7197-2010, 2010.
- 388 15. Motty, G.S., Malladi Satyanarayana, Jayeshlal, G.S., Krishnakumar, V. and Mahadevan
389 Pillai, V.P.: Optical Properties of Cirrus Clouds in the Tropical Tropopause Region during two
390 Contrasting Seasons. *Indian J. of Radio & Space Phys.*, 44, 155–166, 2015.
- 391 16. Motty, G.S., Jayeshlal, G.S., Malladi Satyanarayana and Mahadevan Pillai, V. P.: Lidar studies on
392 climate sensitivity characteristics of tropical cirrus clouds, *Proc. SPIE 9876, Remote Sensing of the
393 Atmosphere, Clouds, and Precipitation VI*, 98761X, doi:10.1117/12.2223301, 2016.
- 394 17. Heymsfield, A. J., McFarquhar, G. M.: High albedos of cirrus in the tropical Pacific warm pool:
395 Microphysical interpretations from CEPEX and from Kwajalein, Marshall Islands. *J. Atmos. Sci.*, 53,
396 2424–2451, 1996.
- 397 18. Prabhakara, C., Kratz, D. P., Yoo, J.-M., Dalu, G. and Vernekar, A.: Optically thin cirrus clouds:
398 Radiative impact on the warm pool, *J. Quant. Spectrosc. Radiat. Transfer*, 49, 467–483, 1993.
- 399 19. Heymsfield, A. J., and Miloshevich, L. M.: Parameterizations for the Cross- Sectional Area and
400 Extinction of Cirrus and Stratiform Ice Cloud Particles, *J. Atmos. Sci.*, 60, 936–956, 2003.
- 401 20. Wang, P.-H., McCormick, M. P., Poole, L. R., Chu, W. P., Yue, G. K., Kent, G. S. and Skeens, K.
402 M.: Tropical high cloud characteristics derived from SAGE II extinction measurements, *Atmos. Res.*,
403 34, 53–83, 1994.
- 404 21. Kulkarni, P., Ramachandran, S., Bhavani Kumar, Y., Narayana Rao, D., and Krishnaiah, M.: Features
405 of upper troposphere and lower stratosphere aerosols observed by lidar over Gadanki, a tropical Indian
406 station, *J. Geophys. Res.-Atmos.*, 113, D17207, doi: 10.1029/2007JD009411, 2008.
- 407 22. Vernier, J.-P., Fairlie, T. D., Natarajan, M., Wienhold, F. G., Bian, J., Martinsson, B. G., Crumeyrolle,
408 S., Thomason, L. W., and Bedka, K.: Increase in upper tropospheric and lower stratospheric aerosol
409 levels and its potential connection with Asian Pollution, *J. Geophys. Res.-Atmos.*, 120, 1608–1619,
410 doi:10.1002/2014JD022372, 2015.
- 411 23. Dessler, A.E.: Clouds and water vapor in the northern hemisphere summertime stratosphere, *J.*
412 *Geophys. Res.*, 114, D00H09, doi: 10.1029/2009JD012075, 2009.
- 413 24. Meenu, S., Rajeev, K. and Parameshwaran, K.: Regional and vertical distribution of semitransparent
414 cirrus clouds and cloud top altitudes over tropical Indian region derived from CALIPSO data,” *J.*
415 *Atmos. Solar-Terr. Phys.* 73(13), 1967–1979, 2011.
- 416 25. Nazaryan, H., McCormick, M. P., and Menzel, W. P.: Global characterization of cirrus clouds using
417 CALIPSO data, *J. Geophys. Res.-Atmos.*, 113, D16211, doi: 10.1029/2007JD009481, 2008.



- 418 26. Sivakumar, V., Bhavanikumar, Y., Rao, P. B., Mizutani, K., Aoki, T., Yasui, M. and Itabe, T.:Lidar
419 observed characteristics of the tropical cirrus clouds, *Radio Sci.*, 38 (6), 1, 2003.
- 420 27. Parameswaran, K. et al.:Lidar observations of cirrus cloud near the tropical tropopause: temporal
421 variations and association with tropospheric turbulence, *Atmos.Res.*69(1–2),29–49,2003.
- 422 28. Krishnakumar, V., et al. : Lidar investigations on the optical and dynamical properties of cirrus clouds
423 in the upper troposphere and lower stratosphere regions at a tropical station, Gadanki, India (13.5°N,
424 79.2°E), *J. Appl. Remote Sens.*,8 (1), 083659,2014.
- 425 29. Winker, D.M., Hunt, W. H. and McGill, M. J.:Initial performance assessment of CALIOP”,
426 *Geophys.Res.Lett.*,34(19), L19,803, 2007.
- 427 30. Winker, D. M.: CALIPSO mission: spaceborne lidar for observation of aerosols and clouds (2003)
428 Winker Publications Spie, in *Proc. SPIE* , Lidar Remote Sensing for Industry and Environment
429 Monitoring III, vol. 4893, available at:
430 <http://spie.org/Publications/Proceedings/Paper/10.1117/12.466539#U7OSke5RVwE.citeulike>, 2003.
- 431 31. Hunt,W. H.,Winker, D. M., Vaughan, M. A., Powell, K. A., Lucker, P. L., and Weimer, C.: CALIPSO
432 lidar description and performance assessment, *J. Atmospheric Ocean. Technol.*, 26, 1214– 1228,
433 doi:10.1175/2009JTECHA1223.1, 2009.
- 434 32. Winker, D. M., Vaughan, M. A., Omar, A., Hu, Y., Powell, K. A., Liu, Z., Hunt, W. H., and Young, S.
435 A.: Overview of the CALIPSO Mission and CALIOP Data Processing Algorithms, *J. Atmospheric*
436 *Ocean. Technol.*, 26, 2310–2323, doi:10.1175/2009JTECHA1281.1, 2009.
- 437 33. Pandit, A. K., Gadhavi, H. S., Venkat Ratnam, M., Raghunath, K., Rao, S. V. B., and Jayaraman, A.:
438 Long-term trend analysis and climatology of tropical cirrus clouds using 16 years of lidar data set over
439 Southern India, *Atmos. Chem. Phys.*, 15, 13833-13848, doi:10.5194/acp-15-13833-2015, 2015.
- 440 34. Fernald, F. G.:Analysis of atmospheric lidar observations: some comments, *Appl. Opt.* 23, 652-
441 653,1984.
- 442 35. Sassen, K. and Cho, B. S.:Subvisual thin cirrus lidar data set for satellite verification and
443 climatological research, *J. Appl. Meteorol.*, 31(11), 1275–1285 (1992), [doi:10.1175/1520-0450].
- 444 36. Bodhaine, B. A. et al.:On Rayleigh optical depth calculations, *J. Atmos. Ocean. Technol.*, 16 (11),
445 1854-1861, 1999.
- 446 37. Satyanarayana, M. et al.:Laser radar characterization of atmospheric aerosols in the troposphere and
447 stratosphere using range dependent lidar ratio, *J. Appl. Remote Sens.* 4(1), 043503 ,
448 <http://dx.doi.org/10.1117/1.3306573>,2010.
- 449 38. Heymsfield, A. J., Winker, D. and van Zadelhoff, G.-J.:Extinction-ice water content-effective radius
450 algorithms for CALIPSO, *Geophys. Res. Lett.*, 32, L10807, doi:10.1029/2005GL022742,2005.
- 451 39. Heymsfield, A.J., Winker, D., Avery, M., Vaughan, M., Diskin, G., Deng, M., Mitev, V. and
452 Matthey, R.: Relationships between ice water content and volume extinction coefficient from in situ
453 observations for temperatures from 0° to -86°C: Implications for spaceborne lidar retrievals, *Journal of*
454 *Applied Meteorology and Climatology*, 53, 479-505, DOI:10.1175/JAMC-D-13-087.1, 2014.
- 455 40. Mitchell, D. L.: Use of mass- and area-dimensional power laws for determining precipitation particle
456 terminal velocities, *J. Atmos. Sci.*, 53, 1710–1723, 1996.



- 457 41. Sunilkumar, S. V., Parameswaran, K. and Thampi, B. V.: Interdependence of tropical cirrus properties
458 and their variability, *Ann. Geophys.* 26, 413–429, 2008.
- 459 42. Seifert, P., Ansmann, A., Müller, D., Wandinger, U., Althausen, D., Heymsfield, A.J., Massie, S.T.,
460 Schmitt, C.: Cirrus optical properties observed with lidar, radiosonde, and satellite over the tropical
461 Indian Ocean during the aerosol-polluted northeast and clean maritime southwest monsoon, *J.*
462 *Geophys. Res.*, 110, D13205, 2007.
- 463 43. Nee, J.B., Len, C. N., Chen, W. N., and Lin, C. I.: Lidar observation of the cirrus cloud in the
464 tropopause at Chung-Li, *J. Atmos. Sci.* 55, 2249–2257, 1998.
- 465 44. Wang, J., Zhang, L., Huang, J., Cao, X., Liu, R. Zhou, B., Wang, H., Huang, Z., Bi, J., Zhou, T.,
466 Zhang, B., Wang, T.: Macrophysical and optical properties of mid-latitude cirrus clouds over a semi-
467 arid area observed by micro-pulse lidar, *Journal of Quantitative Spectroscopy & Radiative Transfer*,
468 122, 3–12, 2013.
- 469 45. Das, S.K., Chiang, C. W. and Nee, J.B.: Characteristics of cirrus clouds and its radiative properties
470 based on lidar observation over Chung-Li, Taiwan, *Atmos. Res.*, 93 (4),
471 723, doi:10.1016/j.atmosres.2009.02.008, 2009.
- 472 46. Chen, W.N., Chiang, C.W. and Nee, J.B.: Lidar ratio and depolarization ratio of Yorks, J. E., D. L.
473 Hlavka, W. D. Hart, M. J. McGill, 2011a: Statistics of Cloud Optical Properties from Airborne Lidar
474 Measurements, *J. Atmos. Oceanic Technol.*, 28, 869–883, 2002.
- 475 47. Grund, C.J., Eloranta, E.W.: The 27–28 October 1986 FIRE IFO cirrus case study: cloud optical
476 properties determined by high spectral resolution lidar, *Mon. Weather Rev.*, 118, 2344–2355, 1990.
- 477 48. Sassen, K. and Comstock, J.: A midlatitude cirrus cloud climatology from the facility for atmospheric
478 remote sensing. Part III: radiative properties, *J. Atmos. Sci.*, 58, 2113–2127, 2001.
- 479 49. Pace, G., Cacciani, M., Sarra, A., Fiocco, G., Fuà, G.: Lidar observations of equatorial cirrus clouds at
480 Mahé Seychelles, *J. Geophys. Res.*, 108 (D8), 4236, 2002.
- 481 50. Giannakaki, E., Balis, D.S., Amiridis, V., Kazadzis, S.: Optical and geometrical characteristics of cirrus
482 clouds over a Southern European lidar station, *Atmos. Chem. Phys.*, 7, 5519–5530, 2007.
- 483 51. Sassen, K.: Lidar cloud research, *Rev. Laser Eng.*, 23 (2), 148–153, 1995.
- 484 52. Platt, C.M.R., Abshire, N.L., McNice, G.T.: Some microphysical properties of an ice cloud from lidar
485 observations of horizontally oriented crystals, *J. Appl. Meteorol.*, 17, 1220–1224, 1978.
- 486 53. Chen, W.N., Chiang, C.W. and Nee, J.B.: Lidar ratio and depolarization ratio for cirrus clouds, *Applied*
487 *Optics*, 41:6470 – 6476, 2002.
- 488 54. Reichardt, J., Reichardt, S., Hess, M. and McGee, T.: Correlations among the optical properties of
489 cirrus-cloud particles: Implications for spaceborne remote sensing, *Journal of Geophysical*
490 *Research*, 107, 8–12, 2002.
- 491 55. Sakai, T., Orikasa, N., Nagai, T., Murakami, M., Kusunoki, K., Mori, K., Hashimoto, A., Matsumura,
492 T. and Shibata, T.: Optical and Microphysical Properties of Upper Clouds Measured with the Raman
493 Lidar and Hydrometeor Videosonde: A Case Study on 29 March 2004 over Tsukuba, Japan, *Journal of*
494 *the Atmospheric Sciences*, 63:2156 – 2166, 2006.
- 495 56. Heymsfield, A. J., Matrosov, S. and Baum, B.: Ice water path-optical depth relationships for cirrus and
496 deep stratiform ice cloud layers, *J. Appl. Meteorol.*, 42, 1369–1390, 2003.



- 497 57. Deng, M., and Mace, G. D.:Cirrus cloud microphysical properties and air motion statistics using cloud
498 radar Doppler moments: Water content, particle size, and sedimentation relationships, Geophys. Res.
499 Lett., 35 (L17808), doi:10.1029/2008GL035054,2008.
- 500 58. Das, S. K., Nee, J. B. and Chiang, C. W.:A LiDAR study of the effective size of cirrus ice crystals
501 over Chung-Li, Taiwan, J. Atmos. Sol. Terr. Phys., 72 (9-10), 781-788,
502 doi:10.1016/j.jastp.2010.03.024,2010.
- 503 59. Kärcher, B., and Lohmann, U.:A parameterization of cirrus cloud formation: Homogeneous freezing of
504 supercooled aerosols, J. Geophys. Res., 107(D2), 4010, doi:10.1029/2001JD000470,2002.
- 505 60. Heymsfeld, J. A., and Iaquinta, J.:Cirrus Crystal Terminal Velocities, J. Atmos. Sci., 57, 916-938,
506 2000.
- 507 61. Chen, S. S.:Diurnal variation and life-cycle of deep convective systems over the tropical Pacific warm
508 pool, Q. J. R. Meteorol. Soc., 123, 357 -388, 1997.

509

510

511

512

513

514

515

516

517

518

519

520

521

522

523

524

525

526

527

528

529

530

531

532

533

534

535

Table 1. Seasonal average value of properties of cirrus clouds derived with ground based lidar



Mid cloud height(km)	Mid cloud temperature(°C)	Optical depth	Depolarisation ratio	Lidar ratio	Effective particle size(µm)	Fall velocity (cm/sec)
17.2	-79.9	0.0173	0.1696	24.21	281.3	34.5
11.84	-49.96	0.55	0.1568	20.64	272.7	33.4
13.99	-70.75	0.05	0.1054	15.01	261.8	32.05
14.71	-70.33	0.15	0.2168	21.84	265.9	32.5
16	-79	0.028	0.3113	12.96	272.4	33.38
14.06	-67.2	0.25	0.0521	20.64	277.1	33.9
11.62	-41.51	0.05	0.0643	17.09	276.4	33.3
13.24	-63.42	0.106	0.0507	23.22	398.5	49.5
14.48	-66.31	0.01393	0.1234	17.63	259.6	31.7
14.38	-63.5	0.012	0.0995	27.16	335.9	41.4
14.66	-68	0.6	0.415	25.11	244.8	29.9
12.93	-64.3	0.25	0.189	23.22	286.6	35.2
14.17	-61.6	0.255	0.0408	26.08	312.9	38.5
14.39	-70.16	0.038	0.0589	22.94	304.6	37.4
14.64	-67.58	0.0106	0.3807	16.63	378.4	46.8
13.86	-64.6	0.0118	0.1026	19.98	264.1	32.3
12.4	-46.34	0.3	0.0418	25.73	360.02	44.6
15.1	-62.3	0.2	0.3239	22.94	262.8	32.18
13.05	-57.15	0.265	0.1505	20.08	316.6	39.01
13.77	-65.66	0.014	0.1182	21.23	377.9	46.79
12.39	-62.5	0.013	0.1176	21.9	288.4	35.42
14.76	-67	0.227	0.131	22.55	263.1	32.29
14.82	-63.75	0.01194	0.0738	25.62	274.6	33.7
14.1	-54.5	0.75	0.1995	21.41	257.5	31.51

536

537

538

539

540

541 **Table 2. Seasonal average value of properties of cirrus clouds derived with satellite based lidar**



Mid cloud height(km)	Mid cloud temperature(°C)	Optical depth	Depolarisation ratio	Lidar ratio	Effective particle size(µm)	Fall velocity (cm/sec)
13.56991	-61.96707	0.44233	0.44072	31.22479	338.37518	44.74023
13.94052	-65.62776	0.23966	0.47192	29.45267	334.79426	44.26388
13.43109	-61.88633	0.60375	0.4447	26.12036	326.65703	43.1413
13.91251	-64.72676	0.97909	0.44007	26.19174	337.61668	44.63188
12.68714	-55.72516	0.37189	0.39678	28.35552	371.51118	49.26096
14.78327	-68.16807	0.28282	0.44113	25.49286	335.54569	44.35372
14.0175	-64.31054	0.79158	0.45619	24.98762	361.22532	47.85666
15.59179	-75.7787	0.06528	0.44678	25.09948	360.13977	47.70968
14.04506	-63.33783	0.57707	0.43175	26.85669	334.43792	44.19976
13.90262	-61.09068	0.61027	0.43411	25.96867	357.97366	47.40541
14.11647	-64.21318	0.93512	0.43742	25.21233	375.99098	49.8676
13.37893	-60.43045	0.89786	0.44775	25.94735	379.87508	50.39671
13.52856	-58.89109	0.73884	0.40346	27.38521	363.94335	48.22065
13.83301	-60.21539	1.0968	0.42088	26.24744	364.1064	48.24252
13.8945	-64.61901	0.55583	0.42907	26.75646	352.39667	46.65443
13.06972	-57.32295	0.64174	0.40611	27.57685	332.45256	43.93023
13.23237	-56.84902	0.38632	0.3553	25.29714	311.68792	41.10485
12.63906	-54.21735	0.59498	0.37918	27.04626	354.66284	46.96083

542

543

544

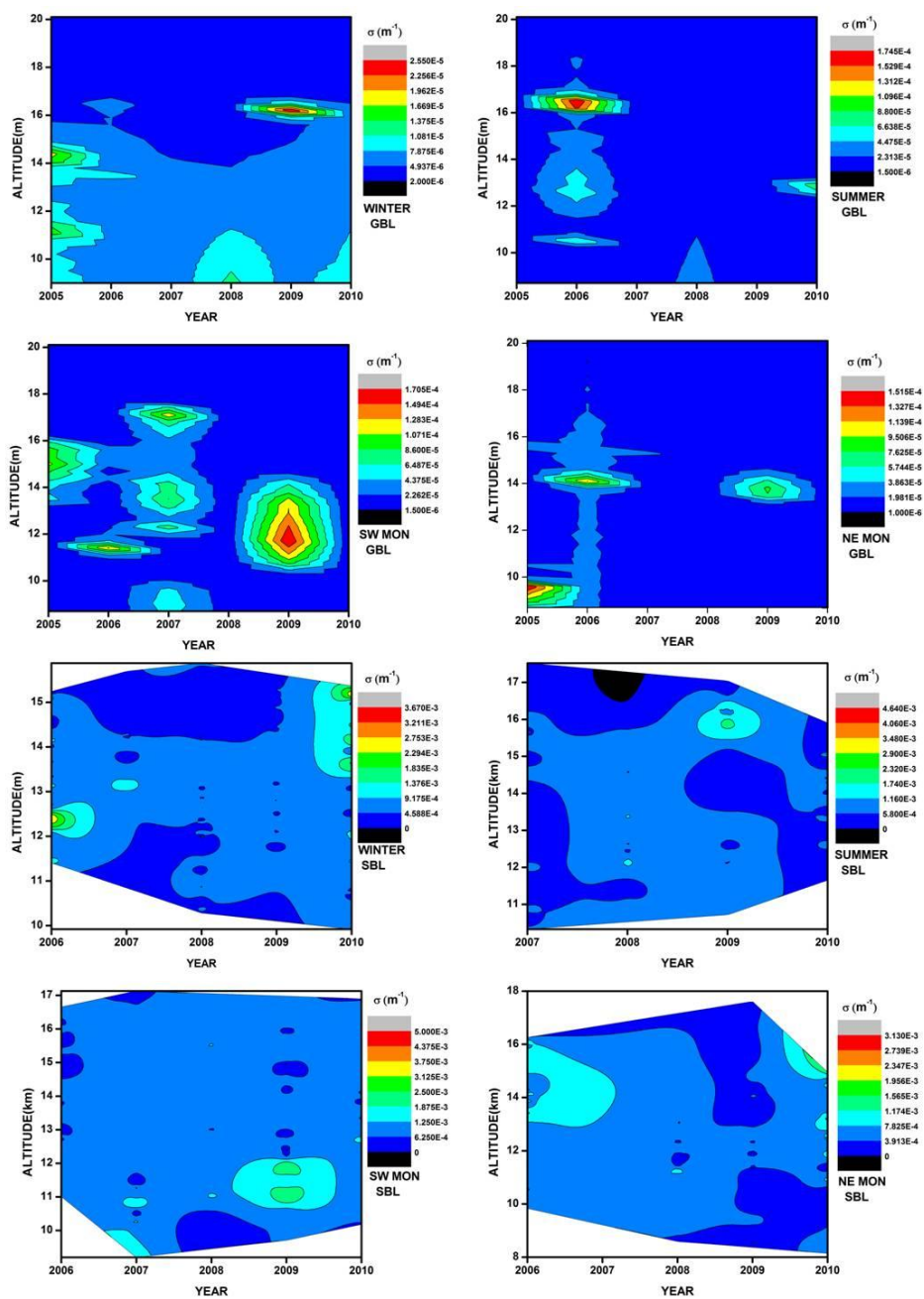
545

546

547

548

549



550

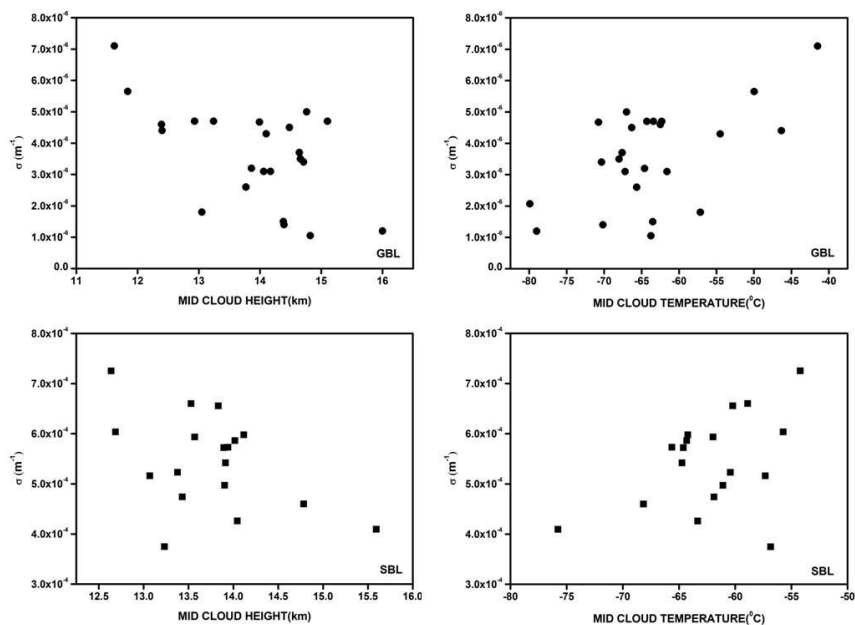
551

552 Figure 1: Contour plot of seasonal variation of Extinction coefficient for (a) ground based lidar (GBL) and (b)
553 satellite based lidar (SBL) observations.

554



555



556

557 **Figure 2: Variation of extinction coefficient according to mid cloud height and mid cloud temperature based on GBL**
558 **and SBL measurement techniques.**

559

560

561

562

563

564

565

566

567

568

569

570

571

572

573

574

575

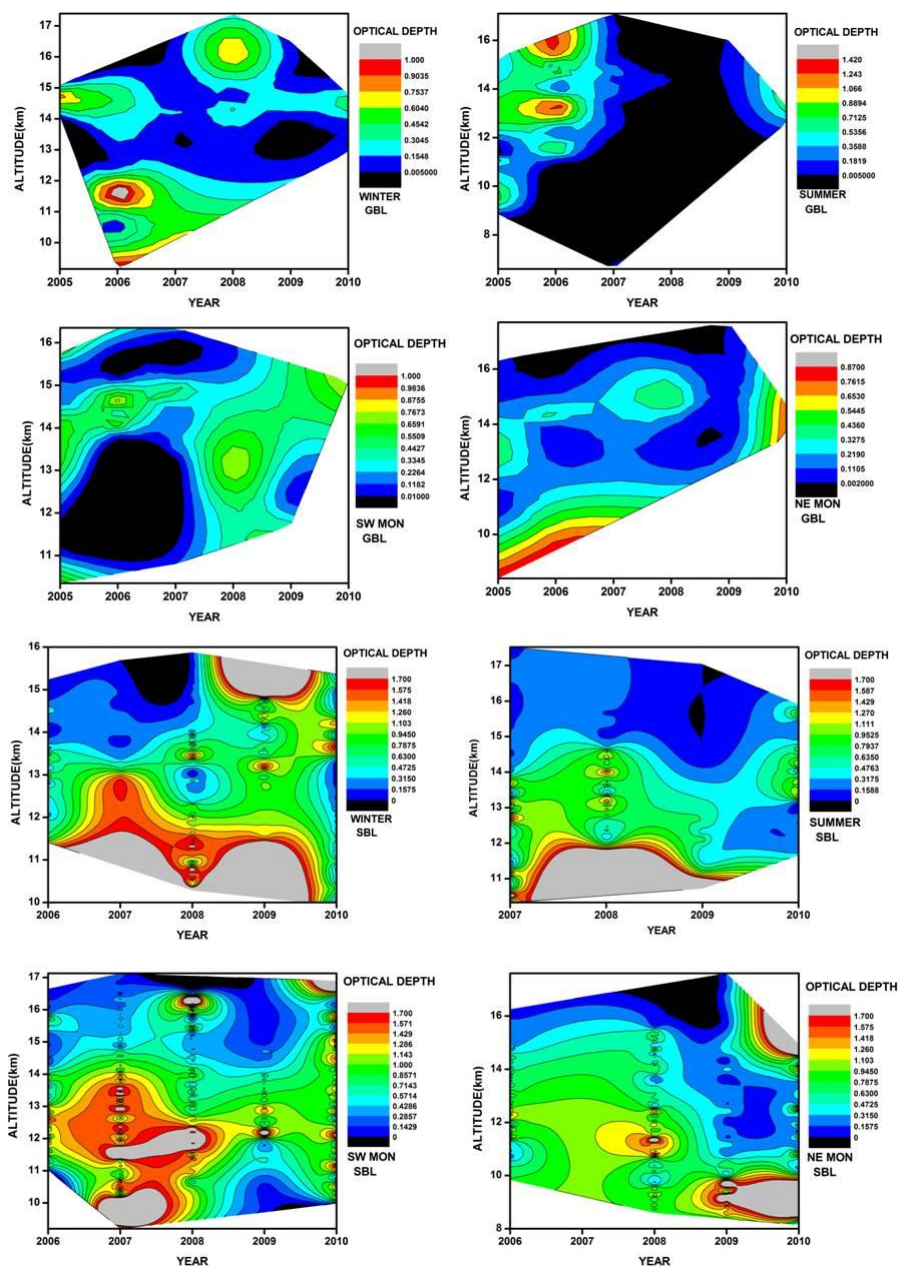
576

577

578



579



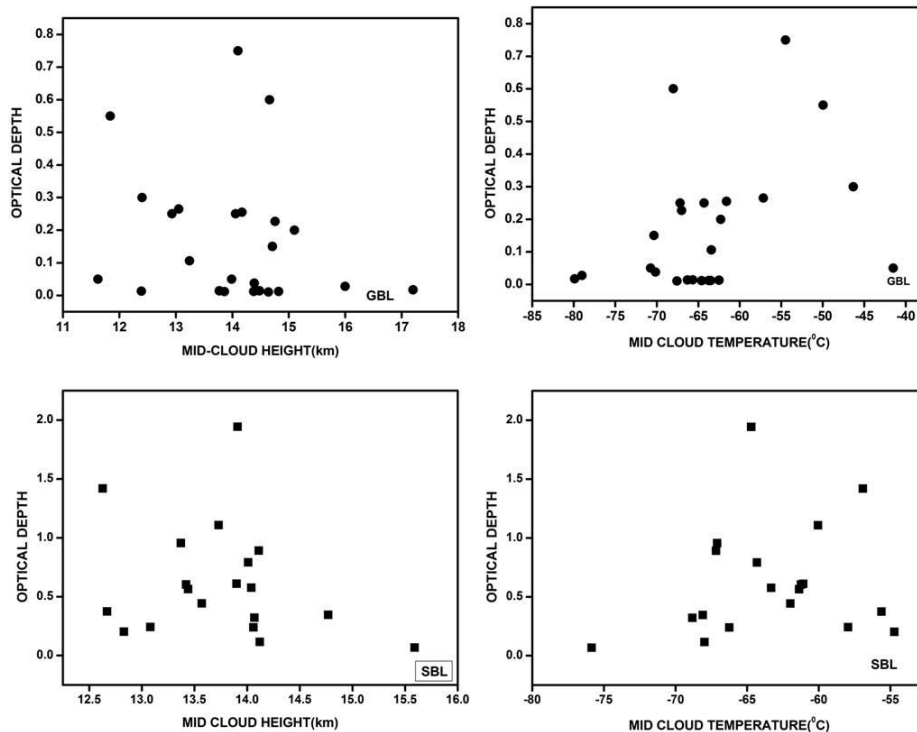
580

581 Figure 3: Contour plot of seasonal variation of optical depth based on GBL and SBL observations.

582

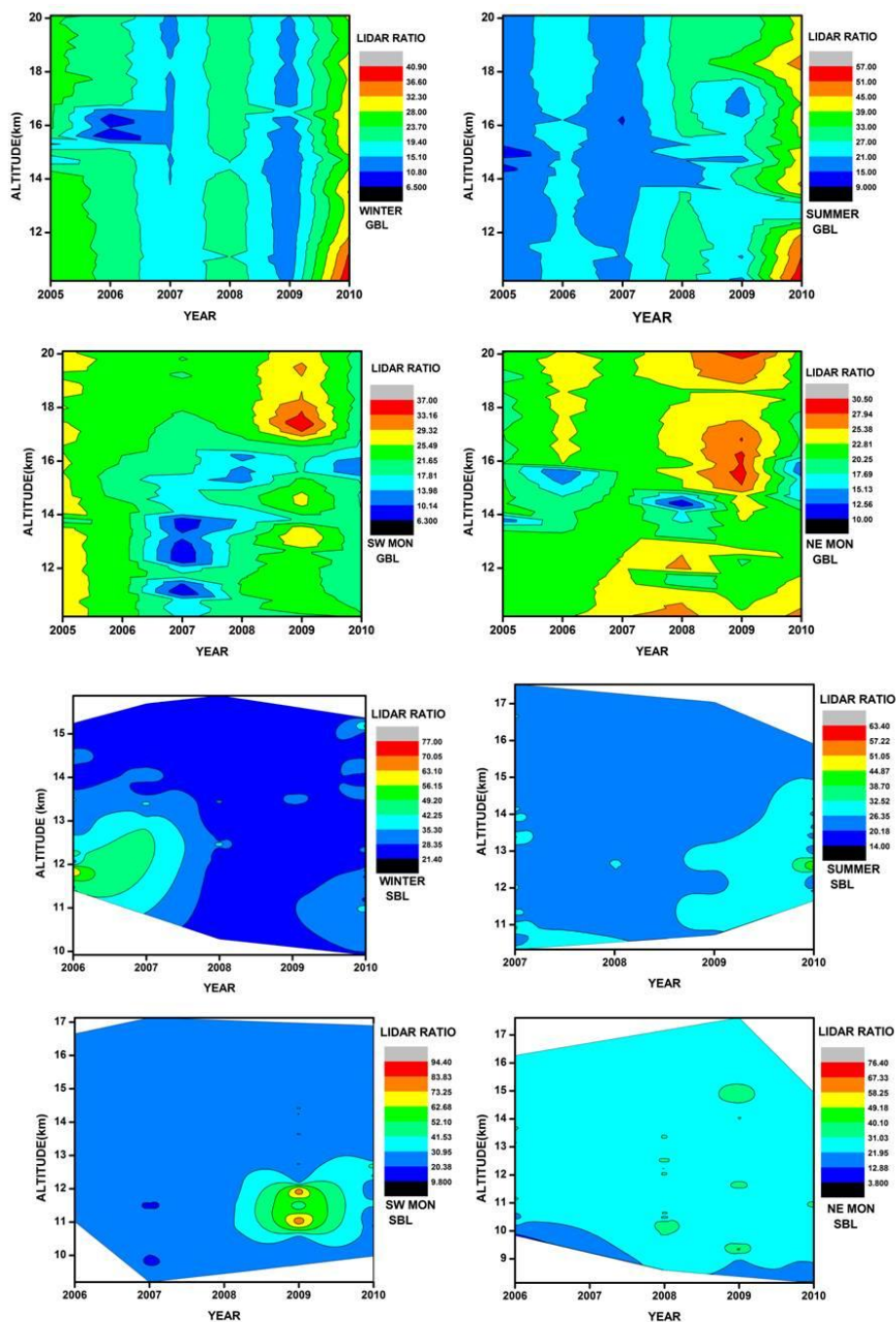
583

584



585
586 **Figure 4: Variation of optical depth according to mid cloud height and mid cloud temperature based on GBL and**
587 **SBL measurement techniques.**

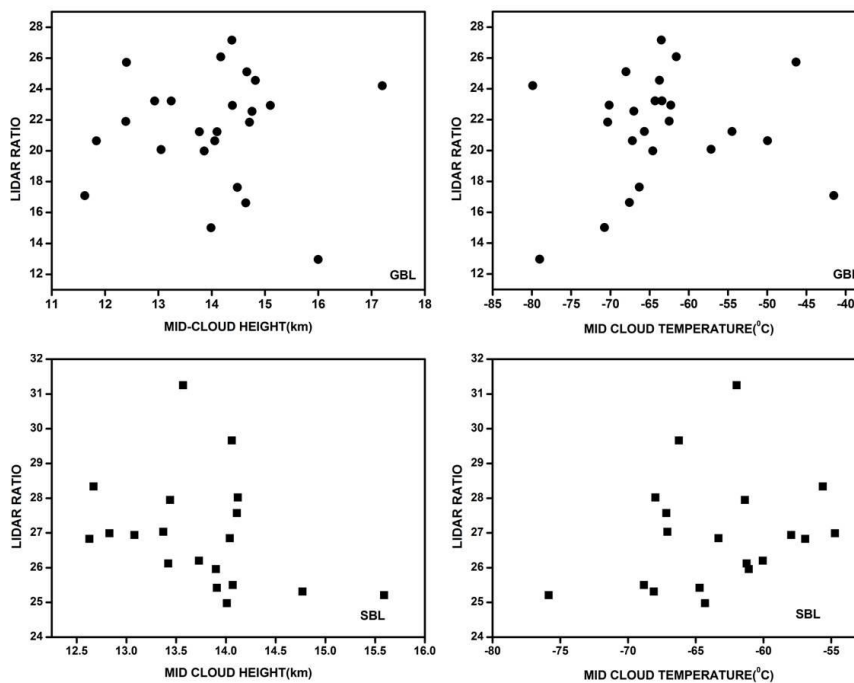
588
589
590
591
592
593
594
595
596
597
598
599
600
601
602
603
604
605



606

607 Figure 5: Counter plot of seasonal variation of Lidar ratio using GBL and SBL observations.

608



609

610 **Figure 6: Variation of Lidar ratio according to mid cloud height and mid cloud temperature based on GBL and SBL**
611 **measurement techniques.**

612

613

614

615

616

617

618

619

620

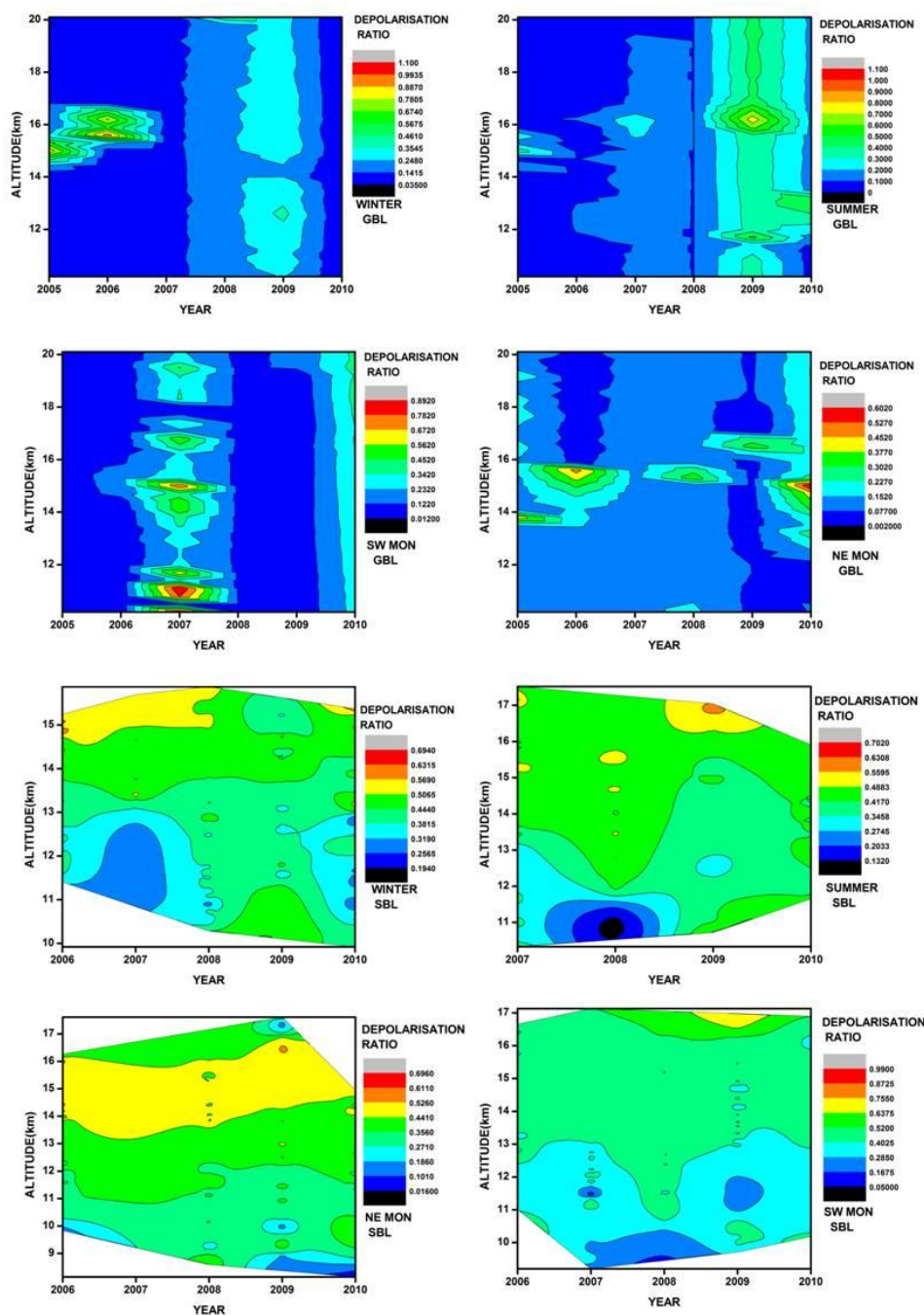
621

622

623

624

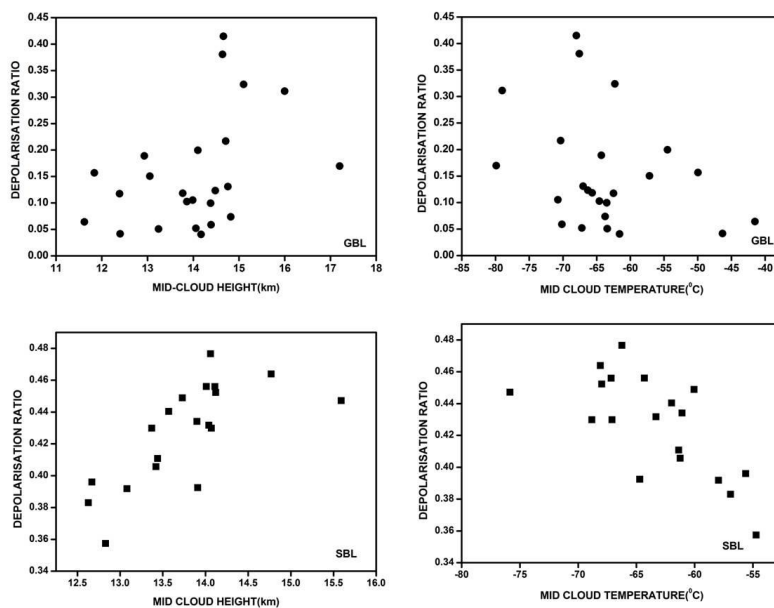
625



626

627 **Figure7: Counter plot of seasonal variation of Depolarisation ratio using GBL and SBL observations.**

628



629

630

Figure 8: Variation of Depolarisation ratio according to mid cloud height and mid cloud temperature based on GBL and SBL measurement techniques.

631

632

633

634

635

636

637

638

639

640

641

642

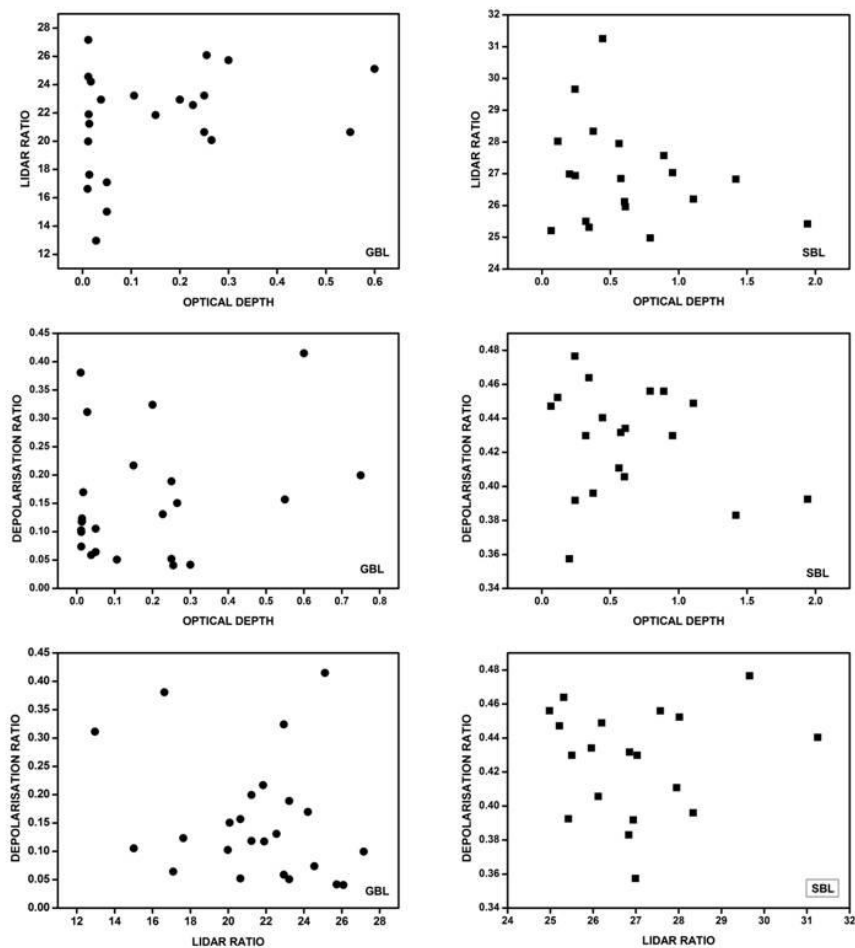
643

644

645

646

647



648

649 **Figure 9: The Inter dependence of (a) Optical depth, (b) Lidar ratio and (c) Depolarisation ratio based on GBL and**
650 **SBL measurement techniques.**

651

652

653

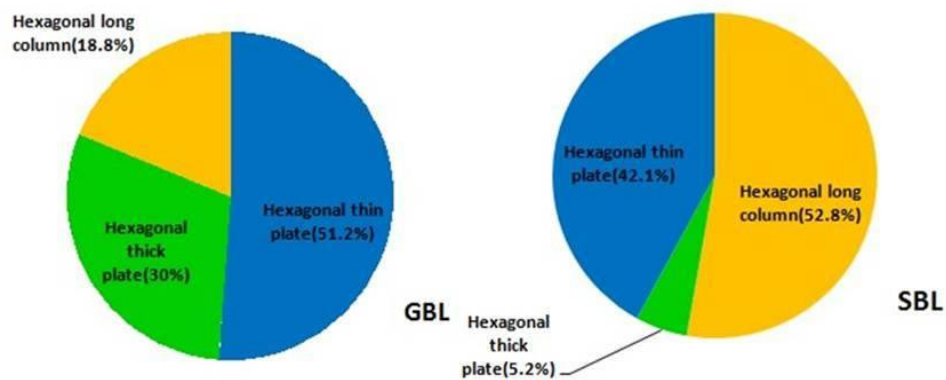
654

655

656

657

658



659

660 **Figure 10: Percent contribution of different types of Hexagonal crystals in the cirrus observations based on the LR**
661 **and DPR values by using Ground based lidar(GBL) and Satellite based lidar (SBL).**

662

663

664

665

666

667

668

669

670

671

672

673

674

675

676

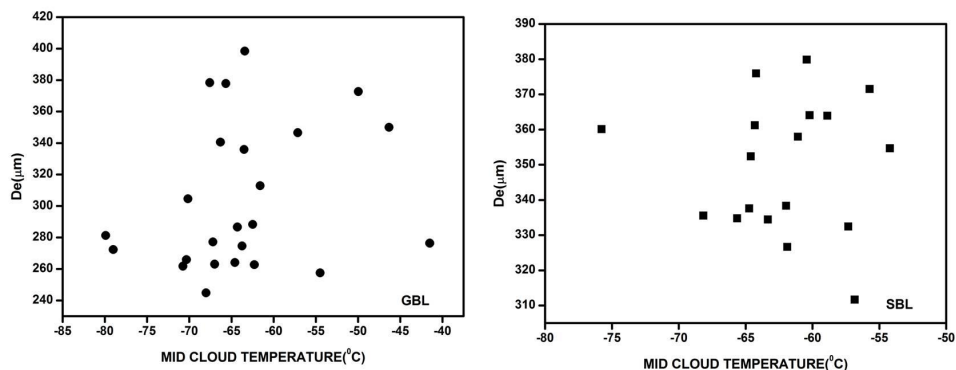
677

678

679

680

681



682

683 **Figure 11: The scatter plot of dependence of effective size of ice particles in cirrus clouds with mid cloud temperature**
684 **by using GBL and SBL.**

685

686

687

688

689

690

691

692

693

694

695

696

697

698

699

700

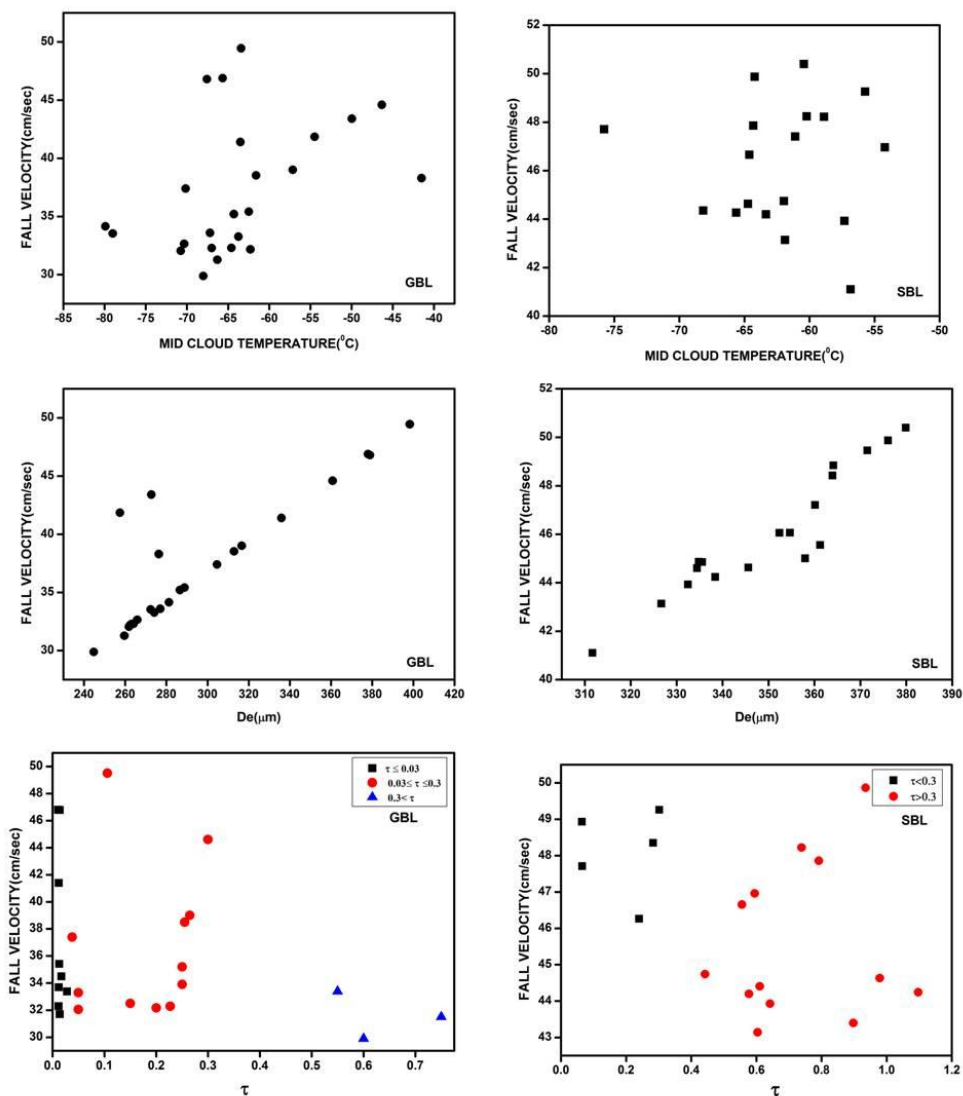
701

702

703

704

705



706

707 Figure 12: Dependence of fall velocity of cirrus cloud particles with mid cloud temperature , effective size and
 708 optical depth by using GBL and SBL.

709

710

711

712

713